World Scientific
www.worldscientific.com

Metal–dielectric hybrid nanoparticle for SERS and optical sensing applications in the near-infrared region

Wei Li*, Debao Wang*, Tongyu Meng†, Wei Zhou*, Jingwei Lv*, Lin Yang*, Wei Liu*, Yan Lv*, Yu Wang*, Paul K. Chu‡ and Chao Liu*,§

*School of Physics and Electronic Engineering,
Northeast Petroleum University, Daqing 163318, China

†Leicester International Institute,
Dalian University of Technology, Dalian 124221, China

‡Departments of Physics, Materials Science and Engineering,
and Biomedical Engineering, City University of Hong Kong,
Tat Chee Avenue, Kowloon, Hong Kong, China
§msm-liu@126.com

To explore the strong coupling between the combined plasmonic mode supported by the metal nanoparticle and the anapole mode of the dielectric nanoparticle, a hybrid metal–dielectric nanoparticle consisting of the combination of silicon and silica together with the gold dimer is designed and analyzed by the finite element method (FEM). Theoretical simulation reveals that the enhanced electric field enhancement reaches 640 and unidirectional scattering with almost zero backscattering at multiple wavelengths is achieved in the far-field region. Moreover, the calculated Purcell factor of 12,193 and sensitivity of 610 nm/RIU of the composite nanoparticle are much higher than those of the single-metal or dielectric nanoparticles. In the end, the impact of different structural parameters on the sensitivity, figure of merit and quality factor is analyzed and described, and the maximum sensitivity, Figure of merit and quality factor are found to be 2360 nm/RIU, 18.4 RIU^{-1} and 19.8 RIU^{-1}. The results reveal a new strategy to develop devices for surface-enhancement Raman scattering (SERS), quantum emitters, and sensors.

Keywords: Nanoparticle; near-field enhancement; SERS; sensors.

1. Introduction

Some of the drawbacks plaguing conventional optics such as the diffraction limit[1,2] have been overcome by nano-plasmonics, consequently enabling researchers to confine light down to the sub-wavelength scales. Noble metals such as gold and silver are common nano-plasmonic materials[3,4] showing unique localized surface plasmon

§Corresponding author.

resonance (LSPR).[5–7] The interplay between light and matter is enhanced due to LSPR further spurring the development of sensors,[8–10] surface-enhancement Raman scattering (SERS),[11,12] quantum emitters,[13] and so on.

Based on the principle that highly matched photons of the incident light and metal electrons can excite LSPR,[14] designing the specific plasmonic nanoparticle is essential to improve the electric field enhancement.[15,16] From the materials perspective, nanoparticles can be divided into three categories: metal nanoparticles, dielectric nanoparticles, and metal–dielectric hybrid nanoparticles. In metal nanoparticles, the high intrinsic radiative losses inevitably lead to strong nonradiative decay which hinders practical applications in the field of nanotechnology.[17,18] Dielectric nanoparticles appear to offer a solution as it has been observed that not only the nonradiative decay rate can be reduced due to its inherent low imaginary part, but also the concurrence of electric and magnetic resonance modes can be facilitated by Mie resonances at the optical frequency.[19–21] Therefore, the coupling between the plasmonic modes of the metallic nanoparticle with the anapole modes of the dielectric nanoparticle is a promising approach for light modulation in the visible spectrum. In other words, hybrid metal–dielectric nanoparticles enhance the interaction between LSPR and Mie-like resonance, thereby producing low material loss and large mode volume.[22] The materials and configurations of nanoparticles produce different degrees of enhancement of the electric field intensity and sensitivity.[23–25] For example, Blechman *et al.* demonstrated that the parameter space generated by the strong coupling effect of the plasma nanocavity array and the WS_2 system provides many degrees of freedom to control the field distribution and enhancement.[26] In addition, several state-of-the-art approaches proposed for plasmonic biosensing, such as toroidal sensors, chiral sensors, and Fano resonances, have also provided strong theoretical guidance in the field of plasma sensing.[27–29] It has been demonstrated that hybrid nanoparticles offer flexibility in manipulating light, but to the best of our knowledge, it is still challenging to engineer a hybrid nanoparticle with enhanced electric field and additional functionalities, and the underlying mechanisms are still unclear.

In this work, a hybrid nanoparticle consisting of the metal (gold dimer) and dielectric (Si and SiO_2 cylinders) components is investigated. We first demonstrate that new modes can be created due to the enhanced coupling between the metal and dielectric structures by comparing multipole decomposition of three different types of nanostructures. Owing to the strong coupling effect, the electric field enhancement is greatly improved. Furthermore, we explore the directional far-field emission of the electric dipole emitters placed near the Au dimer and the effects of different external dielectric materials on the scattering cross-section, thus analyzing the variation of the sensitivity. Finally, different structural parameters are discussed in relation to sensitivity, figure of merit and quality factor. Our results present that benefit from its giant nanoparticle-enhanced electromagnetic field, this hybrid nanoparticle can be suitable for sensor to sense the variation of the medium.

2. Multipole Composition Method

To reveal the coupling mechanism of dielectric and metal materials, the multipole decomposition method is employed to analyze the scattering properties.[30] The multipole decomposition containing the electric dipole moment P_α (ED), magnetic dipole moment M_α (MD), toroidal dipole moment T_α (TD), electric quadrupole moment $Q_{\alpha\beta}^e$ (EQ), and magnetic quadrupole moment $Q_{\alpha\beta}^m$ (MQ) is considered as follows[31,32]:

$$P_\alpha = \frac{1}{iw} \int J_\alpha d^3r, \tag{1}$$

$$M_\alpha = \frac{1}{2c} \int [r \times J]_\alpha d^3r, \tag{2}$$

$$T_\alpha = \frac{1}{10c} \int [(r \cdot J)_{r_\alpha} - 2r^2 J_\alpha] d^3r, \tag{3}$$

$$Q_{\alpha\beta}^e = -\frac{1}{iw} \int \left[r_\alpha J_\beta + J_\alpha r_\beta - \frac{2}{3} \delta_{\alpha\beta}(r \cdot J) \right] d^3r, \tag{4}$$

$$Q_{\alpha\beta}^m = \frac{1}{3c} \int [[r \times J]_\alpha r_\beta + r_\alpha [r \times J]_\beta] d^3r, \tag{5}$$

where r is the positive vector and the subscripts α, $\beta = x, y, z$ denotes the components of EQ and MQ. The term $D = P + \frac{ik_0\varepsilon_d}{C} T$ including the interplay of P (ED) and T (TD) moments, is defined as the total electric dipole moment (TED),[32] and the radiation power I of several multipole moments can be derived as follows[33]:

$$I = \frac{1}{8\pi\varepsilon_0} \left[\frac{2\omega^4}{3c^3}|P_\alpha|^2 + \frac{2\omega^4}{3c^3}|M_\alpha|^2 + \frac{4\omega^5}{3c^4} \text{Im}(P_\alpha * T_\alpha) + \frac{2\omega^6}{3c^5}|T_\alpha|^2 \right.$$
$$\left. + \frac{\omega^6}{20c^5} \sum |Q_{\alpha\beta}^e|^2 + \frac{\omega^6}{20c^5} \sum |Q_{\alpha\beta}^m|^2 \right]. \tag{6}$$

The total scattering cross-section can be derived by[33]

$$C_{\text{sca}} = \frac{I}{I_{\text{inc}}} \tag{7}$$

where I_{inc} is the radiation power of the incident light wave.

Figure 1 presents the schematic illustration of the hybrid nanoparticle. As shown in Fig. 1(a), the gold (Au) dimer consists of two identical wedge-shaped nanoparticles with a horizontal gap (G) of 10 nm. The angle (θ), length (L), height (H), and width (D) of the nano-dimers are 0.24 rad, 125 nm, 10 nm, and 60 nm, respectively. Gold is chosen as the metal part instead of silver or aluminum because it is less reactive in air and has great biocompatibility. Figure 1(b) describes the arrangement of the combination of silicon (Si) and silica (SiO$_2$) cylinders with the same radius R of 300 nm and heights H_1 of 5 nm and H_2 of 100 nm, respectively. The silica cylinder mainly acts as the gain medium to facilitate near-field interactions by enhancing the
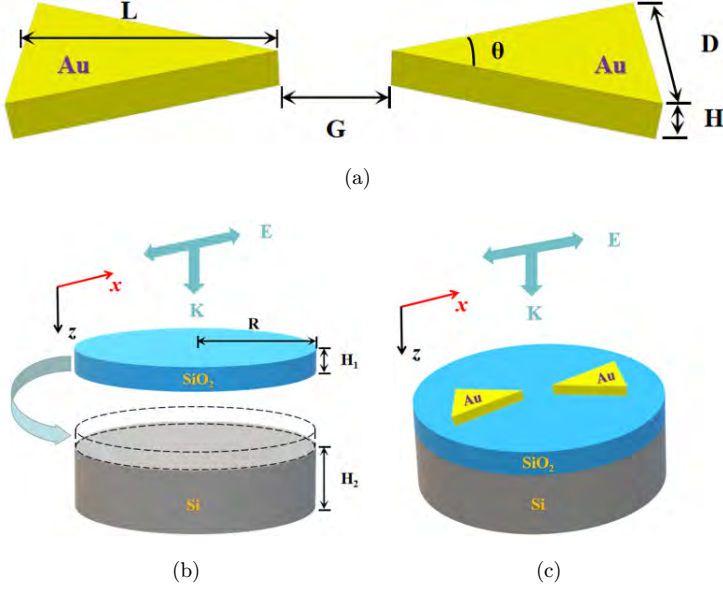
(a)

(b)   (c)

Fig. 1.   (Color online) Schematic illustrations of (a) metal part (gold dimer) and (b) dielectric part (silicon and silica) of the hybrid nanostructure, respectively; (c) structural parameters and arrangement of the hybrid nanostructure under x-polarized excitation by a plane wave.

coupling between the metal and dielectric components.[34,35] The refractive index of silicon is set to $n = 3.5$ and the optical constants of Au and Si are taken from Palik's handbook.[36] Figure 1(c) displays the three-dimensional (3D) model of the hybrid nanoparticle, which is illuminated by a plane wave (k along the z direction) and polarized along the x direction. The hybrid system is assumed to be freestanding in air (refractive index $n = 1.0$). Numerical calculations are carried out by the finite element method (FEM) using the simulation software COMSOL 6.0 Multiphysics. Furthermore, the proposed hybrid nanoparticle can be fabricated by deposition on a substrate, which in turn can be observed by SEM development.[37]

3. Results and Discussion

To investigate the strong coupling between the LSPR resonance and anapole mode, the metal component and dielectric components are studied, as shown in Fig. 2. The electric dipole moment (ED) holds a dominant position in the entire spectrum, indicating that the contributions of other higher-order patterns can be neglected (refer to Fig. 2(a)). There is a resonance peak in the ED moment at the wavelength of 1119 nm originating from the excitation of electrons on the metal surface. The strong electric field is mainly distributed at the tip of the Au dimer as shown in the right inset of Fig. 2(a) due to the lightning rod effect.[38] Figure 2(b) presents the multipolar decompositions of scattering cross-section spectra of the nanoparticle composed of Si and SiO$_2$ at wavelengths ranging from 900 nm to 1800 nm. The dip in the SCS
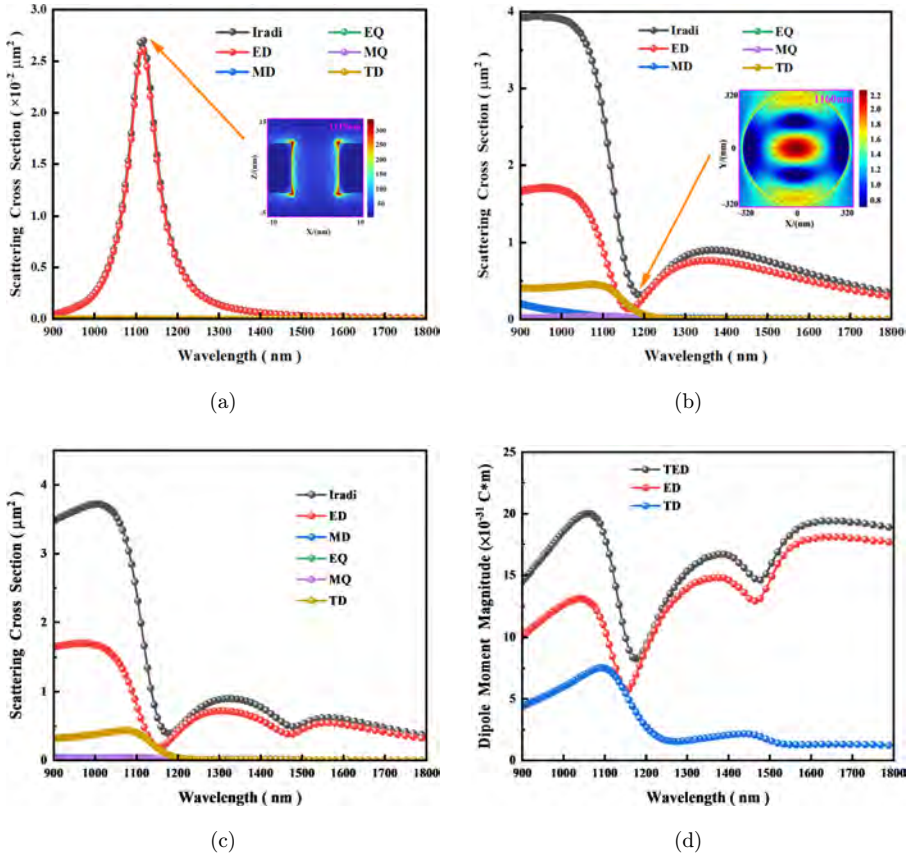
(a)

(b)

(c)

(d)

Fig. 2.   (Color online) ((a)–(c)) Multipolar decompositions of the scattering cross-section spectra of the Au dimer, combination of Si and SiO_2, and hybrid nanostructure, respectively. The right insets in (a) and (b) are the schematic illustrations of the normalized electric field distributions of two simple configurations at wavelengths of 1119 nm and 1160 nm, respectively. (d) Dipolar moments of TED, ED, and TD of the hybrid nanostructure.

spectrum ($\sim$1160 nm) is an electric anapole mode arising from the destructive interference of the ED and TD responses. The electric field distribution in the right inset of Fig. 2(b) reveals a clear dipole mode. The Au dimer is introduced to the upper surface of the dielectric combination to form the hybrid nanoparticle as shown in Fig. 1(c), and the multipole decomposition is shown in Fig. 2(c). In contrast to Figs. 2(a) and 2(b), two dips (at 1175 nm and 1477 nm) of SCS emerge due to the strong coupling between the metal and dielectric components. In other words, these two dips are mainly caused by the spatial overlap and destruction of the ED and TD moments of the hybrid nanoparticle shown in Fig. 2(d). The results show that a new mode (wavelength of 1477 nm) can be generated by the strong coupling effect between the metal and dielectric components. Apart from that, the implementation of the optical anapole modes also offers the possibility of sensing.
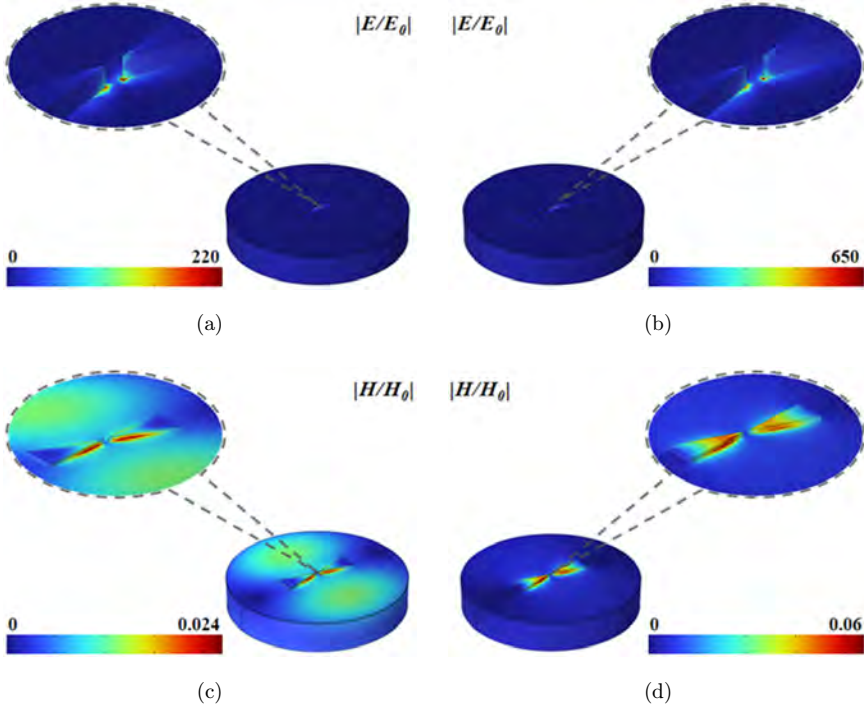
Fig. 3. (Color online) (a) Electric and (c) magnetic field distributions at the first dip at 1175 nm; (b) electric and (d) magnetic field distributions at the second dip at 1477 nm.

To validate our analysis, the distributions of the electric and magnetic fields at both dips (1175 nm and 1477 nm) are displayed in Fig. 3. Figures 3(a) and 3(b) describe the electric fields at the corresponding wavelength with partial enlargement on both sides. The electric field is distributed in the vicinity of the dimer, while the strong electric field is mainly near the top of the dimer. Meanwhile, the electric field at 1477 nm is significantly higher than that at 1175 nm because the ED moment occupies a dominant position in the hybrid nanoparticle. In addition, the hybrid nanoparticle shows two magnetic hotspots on both sides of the surface, as shown in Figs. 3(c) and 3(d).

To study the electric field enhancement effect, the electric fields at different points of the hybrid nanoparticle are presented in Fig. 4. Figure 4(a) describes the relationship between the wavelength and electric field enhancement factor $|E/E_0|$. Five points are selected in the xz-plane as shown in the left inset of Fig. 4(a), namely point A (0,0,0), point B (4.5,0,0), point C (5,0,0), point D (5,0,5) and point E (5,0,10). According to Fig. 4(a), these five points can reach a maximum at 1451 nm. In comparison with the other four points, the largest electric field up to 640 can be obtained at point B. The results indicate that the strong interaction between the Au dimer and dielectric components produces a localized amplified electric field region concentrated on the dielectric surface instead of the tip of the dimer.[39,40] Figure 4(b)
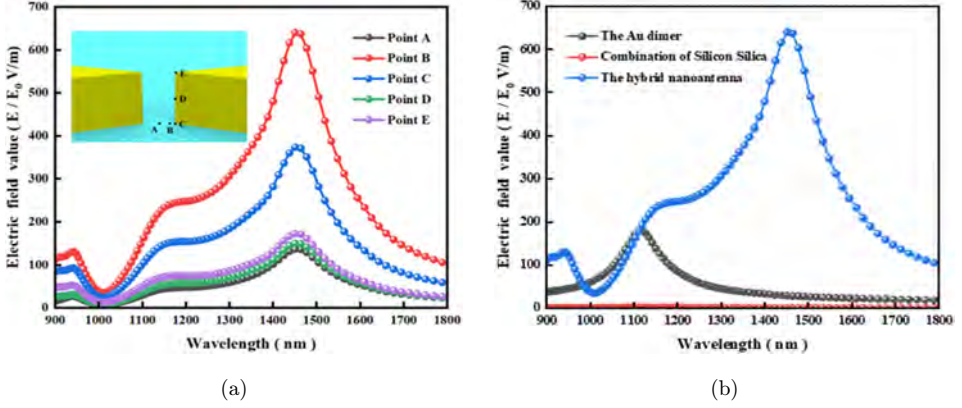
Fig. 4.   (Color online) (a) Electric fields ($|E/E_0|$) of the hybrid nanostructure at different points with the locations shown in the left inset in (a); (b) comparison of the electric fields of the Au dimer, silicon and silica combination, as well as the hybrid nanostructure.

compares the electric fields of the Au dimer, dielectric components, and hybrid nanoparticle. The electric field is significantly stronger than that of other single nanoparticles. The electric field at 1451 nm is 640, which is approximately 3.6 times larger than that of the individual Au dimer in SERS. It can be inferred the hybrid nanoparticle possesses excellent properties such as a high electric field intensity, and it has some positive significance to realize sensing enhancement based on such characteristics.

Furthermore, the radiative properties of the far field are investigated, and the schematic diagram of the two-dimensional (2D) far field at wavelengths of $\lambda = 1060$ nm, $\lambda = 1074$ nm and $\lambda = 1548$ nm is shown in Fig. 5. It can be observed from the figure that the forward scattering (FS) is clearly enhanced and the corresponding backward forward (BS) is suppressed at these three wavelengths, so that it mainly points in the same direction in the middle of the spectrum. It is concluded that the proposed nanoparticle has great directionality.

It has been shown that the substantial enhancement of the electromagnetic field can be utilized to improve the spontaneous emission rate.[41] In this respect, the Purcell factor (PF) plays a significant role in addition to the variations of the field intensity. The total radiative Purcell factor (PF) can be determined by the formula as follows[42]:

$$\mathrm{PF} = \frac{P}{P_0}, \tag{8}$$

$$P_0 = \frac{\omega^4 |P_0|^2}{12\pi\varepsilon_0 c^3}, \tag{9}$$

where P_0 is the vacuum power loss without the resonator and P is the radiation power of the electric dipole emitter with the resonator.

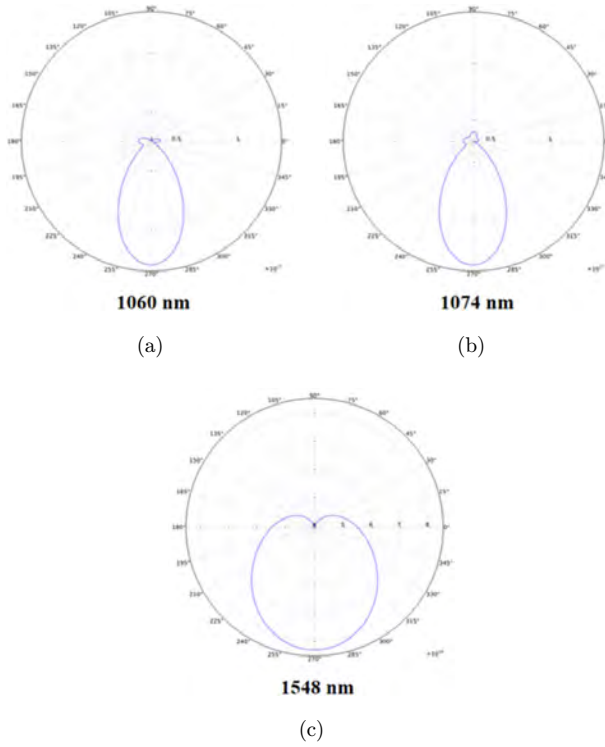1060 nm

(a)

1074 nm

(b)

1548 nm

(c)

Fig. 5.   (Color online) Schematic diagram of the two-dimensional (2D) far field at wavelengths of (a) $\lambda = 1060$ nm, (b) $\lambda = 1074$ nm and (c) $\lambda = 1548$ nm.

Therefore, in order to accurately determine the properties of the proposed structure as a quantum emitter, the Purcell factor at various points on the xz-plane is calculated when the incident light is polarized along the x-axis, as shown in Fig. 6. The spatial coordinates of these points, where the source of an electric dipole is placed (The source points in the x-direction), are graphically represented in the left inset of Fig. 6. Their coordinates are A $(-5,0,10)$, B $(-5,0,0)$, C $(0,0,0)$, D $(5,0,10)$ and E $(5,0,0)$, respectively. The Purcell coefficients of the hybrid nanoparticle at both points C and D (1534 nm and 965 nm) are larger than those at other points. The Purcell factor for inducing plasma states within the system is 12,193, which are approximately 677 and 122 times larger than that of the traditional silicon ED emitter[43] and the combined system consisting of semiconducting single-walled carbon nanotubes with metal nanoelectrodes,[44] respectively.

The effects of different materials on the scattering cross-section are studied and Fig. 7 shows three resonance peaks and two dips at wavelengths from 900 nm to 1900 nm. Both dips move in the direction of the longer wavelengths and the second dip has a bigger line width. The phenomenon can be attributed to the increase in the refractive index and suppressive effect on the coupling between the metal and dielectric components. As a consequence, the scattering cross-section is reduced,
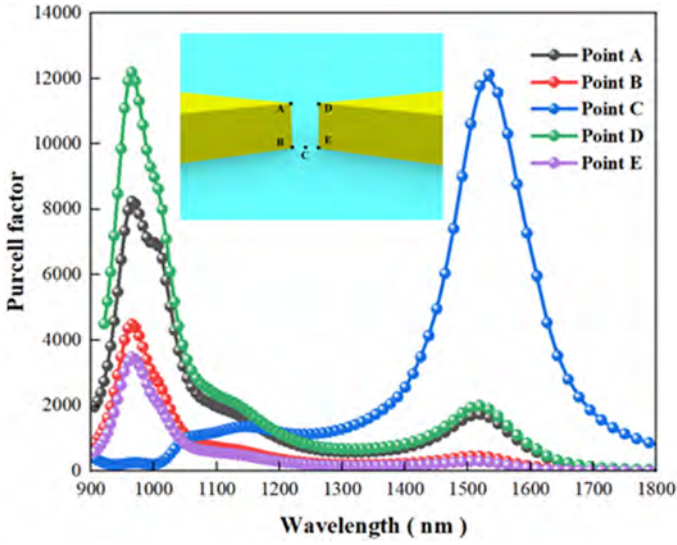
Fig. 6.   (Color online) Purcell factor of the hybrid nanostructure at different points with the inset showing the locations of the five points.
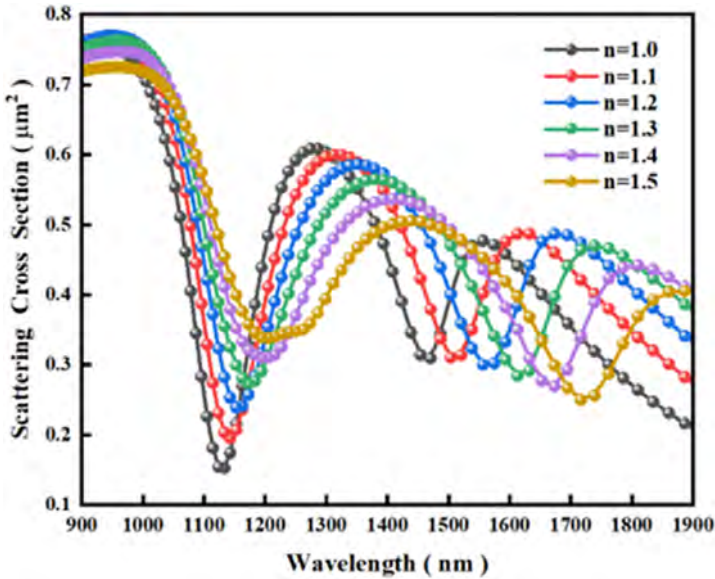

Fig. 7.   (Color online) Effects of different dielectric materials on the scattering cross-sections.

indicating that the nanoparticle is highly sensitive to the variation of the refractive index of the materials and it is feasible as a refractive index sensor.

The sensitivity (S), figure of merit (FOM) and quality factor (Q) of the hybrid nanoparticle are calculated, as shown in Table 1. The sensitivity (S) is defined as

Table 1. Sensitivity (S), figure of merit (FOM) and quality factor (Q) of hybrid nanoparticle made of different dielectric materials.

N	Dips	First dip	Second dip	N	Dips	First dip	Second dip
$n = 1.0$	—	—	—	$n = 1.3$	$\Delta\lambda$	20	57
					FWHM	146	100
					S	200	570
					FOM	1.3	5.7
					Q	8	16.1
$n = 1.1$	$\Delta\lambda$	10	33	$n = 1.4$	$\Delta\lambda$	31	61
	FWHM	136	114		FWHM	126	138
	S	100	330		S	310	610
	FOM	0.7	2.8		FOM	2.4	4.4
	Q	8.3	13.1		Q	9.4	12.1
$n = 1.2$	$\Delta\lambda$	10	52	$n = 1.5$	$\Delta\lambda$	1	43
	FWHM	140	124		FWHM	156	110
	S	100	520		S	10	430
	FOM	0.7	4.1		FOM	0.06	3.9
	Q	8.2	12.5		Q	7.6	15.6

the ratio of the change in the wavelength to the change in the refractive index as shown by[45]

$$S(\mathrm{nm/RIU}) = \Delta\lambda/\Delta n. \tag{10}$$

The figure of merit FOM is defined as the ratio of the change on sensitivity to the change on FWHM as presented by[45]

$$\mathrm{FOM}(\mathrm{RIU}^{-1}) = S/\mathrm{FWHM}. \tag{11}$$

In addition, the quality factor Q can be calculated as[46]

$$Q(\mathrm{RIU}^{-1}) = \lambda/\omega_{\mathrm{FWHM}}. \tag{12}$$

Theoretically, it can be observed from Eq. (10) that increasing the variation of wavelength within a small refractive index fluctuation has a positive effect on the sensitivity. The theoretical analysis of the sensitivity formula is equally applicable to the analysis of the figures of merit (FOM) and quality factor Q. According to Table 1, the maximum sensitivity (S) and FOM are 610 nm/RIU and 4.4 RIU^{-1} at the second dip when the refractive index is $n = 1.4$, which is higher than that of the nanostructure of elliptical and MMI waveguide,[47] confirming the good sensing properties of our nanoparticle. In addition, the quality factor Q at this point is 12.1. This result indicates that the sensing performance at this refractive index is significantly better overall.

The field intensity can be enhanced by varying the structural dimensions of the nanostructure, making it possible to alter the sensitivity.[48] Therefore, the sensitivity of the different heights and gaps of the Au dimer is studied. Figures 8(a) and 8(c)
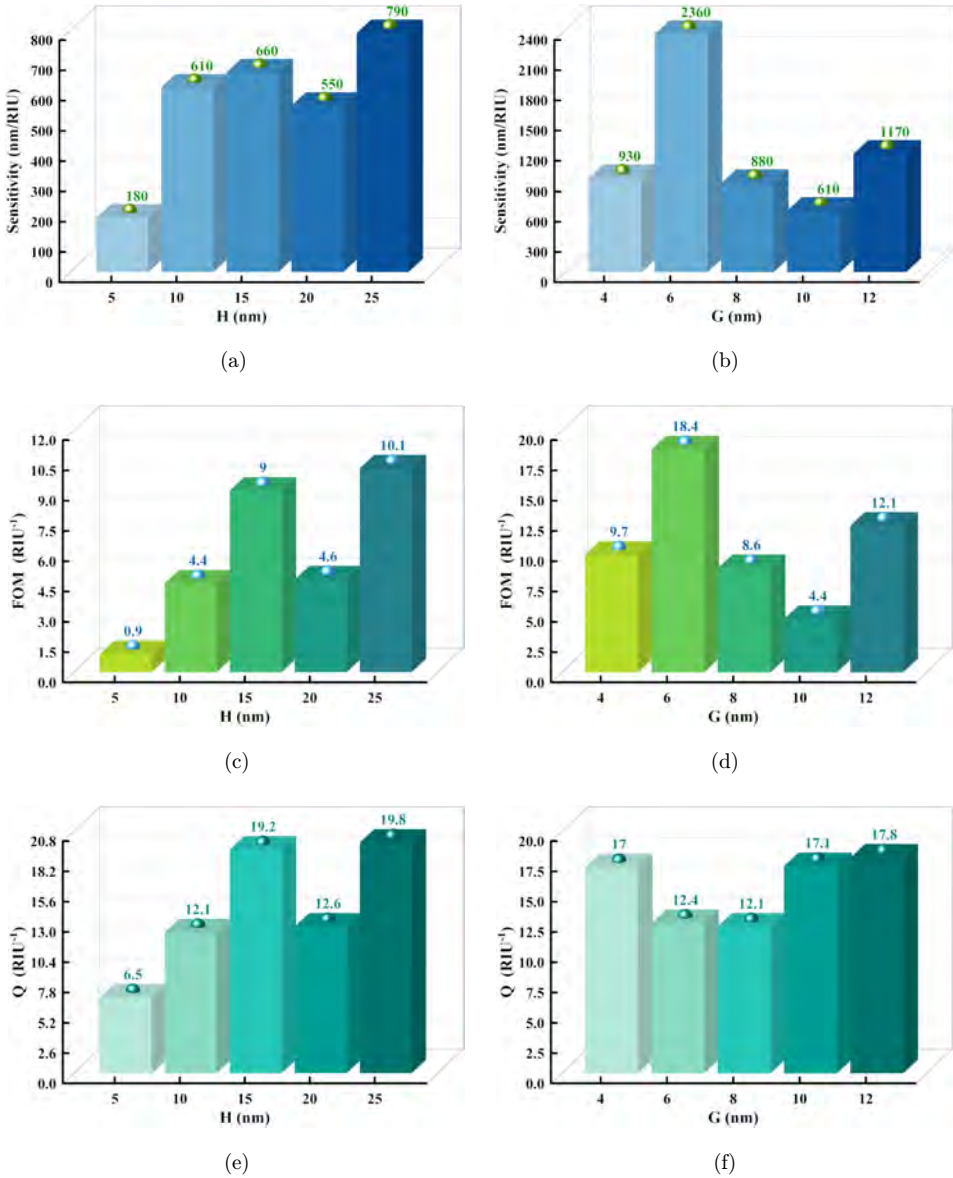
Fig. 8. (Color online) ((a), (c) and (e)) Comparison of the sensitivity, figure of merit and quality factor of different gold dimer heights; ((b), (d) and (f)) comparison of the sensitivity, figure of merit and quality factor of different gold dimer gaps.

present the sensitivity and FOM of the hybrid nanoparticle when the height of the Au dimer H is changed from 5 nm to 25 nm. The trend of the curve of sensitivity is exactly the identical to that of FOM, both of which show an upward tendency and then a downward trend with heights. The highest sensitivity and FOM, 790 nm/RIU

and 10.1 RIU^{-1}, respectively, are obtained at the height of 25 nm. Similarly, the sensitivity and FOM dependence on the separation are shown in Figs. 8(b) and 8(d). The highest sensitivity and FOM are achieved at nearly 2360 nm/RIU and 18.4 RIU^{-1} when the gap $G = 6$ nm. It is significantly stronger than the sensitivity and FOM observed from other gaps. In addition, the variation of the quality factor Q with the dimer height and gap is also presented in Figs. 8(e) and 8(f). The observed relationship between variations in dimer height and the quality factor demonstrates a strong correlation with both sensitivity and figure of merit (FOM) obtaining a maximum value of 19.8 at the height of 25 nm. As for the variation of dimer gap, the quality factor shows a tendency of decreasing and then increasing. The maximum value 17.8 occurs when the gap is 12. Therefore, it can be stated that the height of 25 nm yields a notable enhancement in optical sensing performance. The results reveal that the sensitivity, figure of merit and quality factor are sensitive to structural parameters such as the height and the gap of the dimer.

4. Conclusion

A hybrid nanoparticle made of the gold (Au) dimer and a combination of cylindrical longitudinal Si and SiO_2 is designed. The optical characteristics including the electric field, Purcell factor, and sensitivity are investigated by the finite element method (FEM) in the near-infrared region. The results show that the electric field intensity is improved and the enhancement of electric field intensity in the vicinity of the dimer tip is 640, which is about 3.6 times larger than that of the individual gold dimer nanoparticle. Furthermore, the property of far-field radiation is also evaluated indicating this nanoparticle has great directionality. In addition, the Purcell factor (PF) that gauges the performance of quantum emitters is calculated to be 12,193. The nanoparticle also has a high sensitivity (S) of 610 nm/RIU which is 1.2 times that of the individual dimer. The improvement of sensitivity, figure of merit and quality factor can be tailored by structural parameters. The results show that the hybrid nanoparticle has improved electric field intensity, Purcell factor, as well as sensitivity, boding well for applications are related to SERS, quantum emitters, and sensing.

References

1. N. I. Zheludev, *Nat. Mater.* **7**(6) (2008) 420.
2. M. K. Song, Y. P. Ma, H. Liu, P. P. Hu, C. Z. Huang and J. Zhou, *Anal. Chem.* **94**(11) (2022) 4610.
3. K. Frischwasser, K. Cohen, S. Tsesses, S. Dolev, G. Rosenblatt and G. Bartal, *Phys. Rev. Lett.* **128**(10) (2022) 103901.
4. W. Liu, C. J. Hu, L. Zhou, Y. Zao, C. Liu, J. W. Lv, L. Yang and P. K. Chu, *Physica E Low Dimens. Syst. Nanostruct.* **138** (2022) 115106.
5. J. X. Liu, H. L. He, D. Xiao, S. T. Yin, W. Ji, S. Z. Jiang, D. Luo, B. Wang and Y. J. Liu, *Materials* **11** (2018) 1833.
6. J. W. Lv, D. B. Wang, C. Liu, J. X. Wang, L. Yang, W. Liu, Q. Liu, H. W. Mu and P. K. Chu, *Coatings* **12**(9) (2022) 1248.
7. P. S. S. Dos Santos, J. P. Mendes, B. Dias, J. Perez-Juste, J. M. M. M. De Almeida, I. Pastoriza-Santos and L. C. C. Coelho, *Sensors* **23** (2023) 1666.
8. W. Liu, C. J. Hu, L. Zhou, Z. Yi, Y. Shi, C. Liu, J. W. Lv, L. Yang and P. K. Chu, *Mod. Phys. Lett. B* **36** (2022) 2150499.
9. W. Liu, Y. Shi, Z. Yi, C. Liu, F. M. Wang, X. L. Li, J. W. Lv, L. Yang and P. K. Chu, *Opt. Express* **29** (2021) 40734.
10. J. R. Mejia-Salazar and O. N. Oliveira Jr., *Chem. Rev.* **118**(20) (2018) 10617.
11. A. Mukherjee, Q. Liu, F. Wackenhut, F. Dai, M. Fleischer, P-M. Adam, A. J. Meixner and M. Brecht, *Molecules* **27**(16) (2022) 5097.
12. Y. T. Feng, M. Gao, Y. Wang, L. Y. Meng and M. T. Sun, *J. Raman Spectrosc.* **51** (2020) 476.
13. A. Nodar, T. Neuman, Y. Zhang, J. Aizpurua and R. Esteban, *Opt. Express* **31** (2023) 10297.
14. J. W. Lv, D. B. Wang, C. Liu, Q. Liu, J. X. Wang, L. Yang, H. W. Mu and P. K. Chu, *Chin. Opt.* **16**(1) (2023) 214.
15. K. Trofymchuk, K. Kolataj, V. Glembockyte, F. J. Zhu, G. Acuna, T. Liedl and P. Tinnefeld, *ACS Nano* **17**(2) (2023) 1327.
16. J. Y. Hu, W. D. Bai, C. X. Tan, Y. M. Li, Q. Lin and L. L. Wang, *Opt. Commun.* **511** (2022) 127987.
17. U. Bhattacharjee, C. A. West, S. A. Hosseini Jebeli, H. J. Goldwyn, X. T. Kong, Z. W. Hu, E. K. Beutler, W. S. Chang, K. A. Willets, S. Link and D. J. Masiello, *ACS Nano* **13**(8) (2019) 9655.
18. W. Q. Zhu, R. Esteban, A. G. Borisov, J. J. Baumberg, P. Nordlander, H. J. Lezec, J. Aizpurua and K. B. Crozier, *Nat. Commun.* **7** (2016) 11495.
19. T. C. Huang, B. X. Wang and C. Y. Zhao, *J. Phys. D. Appl. Phys.* **52** (2019) 445102.
20. C. Zaza, L. Violi, J. Gargiulo, G. Chiarelli, L. Schumacher, J. Jakobi, J. Olmos-Trigo, E. Cortes, M. Konig, S. Barcikowski, S. Schlucker, J. Saenz, S. Maier and F. Stefani, *ACS Photonics* **6** (2019) 815.
21. B. Liu, M. L. Hu, Y. W. Zhang, Y. You, Z. G. Liang, X. N. Peng and Z. J. Yang, *Chinese Phys. B* **31** (2022) 057802.
22. S. Sun, D. C. Wang, Z. Feng and W. Tan, *Nanoscale* **12** (2020) 22289.
23. S. L. Li, L. D. Zhou, M. C. Panmai, J. Xiang and S. Lan, *Nanophotonics* **10**(10) (2021) 2639.
24. L. Sabri, Q. L. Huang, J. N. Liu and B. Cunningham, *Opt. Express* **27**(5) (2019) 7196.
25. H. Sugimoto and M. Fujii, *ACS Photonics* **5**(5) (2018) 1986.
26. Y. Blechman, S. Tsesses, G. Feinberg, A. Hayat and G. Bartal, Optimizing the strong coupling of excitons in 2D materials and surface plasmon lattice resonances, *Conf. Lasers and Electro-Optics (CLEO)* (2020), pp. 1–2.

27. Y. Luo, C. Chi, M. Jiang, R. Li, S. Zu, Y. Li and Z. Fang, *Adv. Opt. Mater.* **5**(6) (2017) 1700040.
28. Y. Y. Lee, R. M. Kim, S. W. Im, M. Balamurugan and K. T. Nam, *Nanoscale* **12**(1) (2020) 58.
29. A. Ahmadivand, B. Gerislioglu, R. Ahuja and Y. K. Mishra, *Mater. Today* **32** (2020) 108.
30. D. C. Huang, S. L. Liu, W. Li, K. Yang and T. Peng, *Nanomaterials* **12**(12) (2022) 2084.
31. X. M. Zhang, Q. Zhang, Y. J. Yuan, J. P. Liu and L. X. Liu, *Phys. Lett. A* **384**(27) (2020) 126696.
32. A. B. Evlyukhin, C. Reinhardt, E. Evlyukhin and B. N. Chichkov, *J. Opt. Soc. Am. B* **30** (2013) 2589.
33. C. W. Xu, K. Y. Cheng, Q. Li, X. B. Shang, C. Wu, Z. Y. Wei, X. M. Zhang and H. Q. Li, *AIP Adv.* **9**(7) (2019) 075121.
34. D. Ray, T. V. Raziman, C. Santschi, D. Etezadi, H. Altug and O. Martin, *Nano Lett.* **20**(12) (2020) 8752.
35. D. Ray, A. Kiselev and O. J. F. Martin, *Opt. Express* **29**(15) (2021) 24056.
36. E. D. Palik, *Handbook of Optical Constants of Solids* (Academic Press, New York, 1985), pp. 286–295.
37. D. Wang, X. Fan, W. Fang and H.-J. Niu, *Opt. Express* **31**(6) (2023) 10805.
38. N. Macia, R. Bresoli-Obach, S. Nonell and B. Heyne, *J. Am. Chem. Soc.* **141** (2019) 684.
39. J. Wen, H. Wang, W. Wang, Z. Deng, C. Zhuang, Y. Zhang, F. Liu, J. She, J. Chen, H. Chen, S. Deng and N. Xu, *Nano Lett.* **17**(8) (2017) 4689.
40. J.-N. Liu, Q. Huang, K.-K. Liu, S. Singamaneni and B. T. Cunningham, *Nano Lett.* **17** (2017) 7569.
41. D. Rocco, A. Lamprianidis, A. Miroshnichenko and C. De Angelis, *J. Opt. Soc. Am. B* **37**(9) (2020) 2738.
42. J. W. Lv, H. W. Mu, Q. Liu, X. M. Zhang, X. L. Li, C. Liu, S. S. Jiang, T. Sun and P. K. Chu, *Appl. Opt.* **57**(17) (2018) 4771.
43. Q. R. Deng, J. F. Chen, L. Li, B. Q. Chen, H. K. Yu and Z. Y. Li, *Opto-Electron. Adv.* **5** (2022) 210024.
44. A. Ahmadivand, *J. Phys. Chem. C* **125**(1) (2021) 782.
45. W. Liu, C. Liu, J. X. Wang, J. W. Lv, Y. Lv, L. Yang, N. An, Z. Yi, Q. Liu, C. J. Hu and P. K. Chu, *Results Phys.* **47** (2023) 106365.
46. S. Yuan, X. Z. Qiu, C. C. Cui, L. Q. Zhu, Y. X. Wang, Y. Li, J. W. Song, Q. Z. Huang and J. S. Xia, *ACS Nano* **11**(11) (2017) 10704.
47. S. Khani and M. Hayati, *Superlattices Microstruct.* **156** (2021) 106970.
48. S. Verma and B. M. A. Rahman, *Sensors* **23**(3) (2023) 1290.